RSC Advances

PAPER

View Article Online
View Journal | View Issue

Cite this: *RSC Adv.*, 2024, **14**, 36161

Investigation of variable range hopping and dielectric relaxation in $GdCrO_3$ orthochromite perovskites

Mohamed Youssef Gneber,[a] Imen Elhamdi,[a] Jalel Messoudi,[a] Radhia Dhahri,[a] Foudil Sahnoune,[b] Mosbah Jemmali,[cd] Magdy Hussein,[e] Essebti Dhahri[a] and Benilde Faria Oliveira Costa[f]

This study investigates the structural, electrical, and dielectric properties of $GdCrO_3$ (GCO) compounds. X-ray diffraction analysis confirmed the formation of the perovskite phase of GCO, crystallizing with the *Pbnm* space group. Scanning electron microscopy (SEM) was employed to examine the morphology and chemical composition of the powder, ensuring compound homogeneity, while transmission electron microscopy (TEM) provided insights into the internal structure and finer morphology of the GCO sample. Electrical measurements revealed that GCO exhibits semiconductor behavior, with a notable increase in conductivity as temperature rises, attributed to enhanced charge carrier mobility and hopping conduction mechanisms. Dielectric analysis demonstrated significant frequency-dependent behavior, characterized by various polarization effects and relaxation phenomena. GCO is a promising material for energy storage due to its giant permittivity and low energy loss. The activation energies derived from the electrical and dielectric measurements indicate higher resistance within the grains compared to the grain boundaries, suggesting complex conduction processes. Additionally, the dielectric loss spectra revealed substantial losses, likely due to defect states such as oxygen vacancies and mixed valence states, indicating a highly disordered material. These comprehensive insights into the structural and functional properties of GCO highlight its potential applications in electronic and electrical devices where controlled conductivity and dielectric properties are crucial.

Received 22nd August 2024
Accepted 18th October 2024

DOI: 10.1039/d4ra06104g

rsc.li/rsc-advances

1 Introduction

In recent years, perovskite oxides have been widely studied due to their increasing importance in both research and technology.[1–4] Among these, rare-earth chromites ($ACrO_3$, where A represents elements such as La, Gd, and Nd) have attracted considerable interest. This is due to their diverse physical properties, including multiferroicity,[5] photocatalysis,[6] magnetization reversal[7] exchange bias,[8] and the coupling of electric and magnetic dipoles at low temperatures.[9] Therefore, rare-earth perovskite chromites have found extensive use in various technological applications. These include catalysts,[10] volatile memories,[11] oxygen ion conductors,[12] solid oxide fuel cells,[13] sensors,[14] magnetic refrigerators,[15] and interconnectors in multiferroic devices.[16] Their effectiveness is particularly influenced by the R-site-dependent canted ferroelectric and antiferromagnetic properties. $GdCrO_3$ (GCO), a rare-earth perovskite chromite, has been extensively studied due to its exceptional optical, dielectric, electrical, magnetic and magnetocaloric properties. These characteristics have positioned GCO as a versatile candidate in various applications including photocatalytic reduction,[17] photocatalytic hydrogen evolution,[18] magnetic refrigeration[19] supercapacitors,[20] and spintronics.[21] The magnetic properties of GCO stem from interactions involving Cr^{3+}–Cr^{3+}, Gd^{3+}–Gd^{3+}, and Cr^{3+}–Gd^{3+} pairs, which exhibit temperature-dependent behavior.[22]

GCO exhibits a distorted perovskite structure at room temperature with space group *Pbnm*.[23] In its orthorhombic crystal lattice, gadolinium ions occupy the corners of the unit cell, while chromium ions are situated at the central positions. In the orthorhombic phase of rare-earth chromite's, there is notable magnetic and electric dipolar coupling at low temperatures, which is critical for advancing magnetic and ferroelectric device technologies.[24] Interestingly, below a certain temperature, nearly all $ACrO_3$ compounds are expected to exhibit the magnetoelectric effect due to their lack of inversion symmetry. This effect results

[a]*Laboratoire de Physique Appliquée, Faculté des Sciences, Université de Sfax, B.P. 1171, 3000 Sfax, Tunisia. E-mail: imen85356@gmail.com*
[b]*Physics and Chemistry of Materials Lab, Faculty of Science, University Mohamed Boudiaf of M'sila, 28000, Algeria*
[c]*Department of Chemistry, College of Science, Qassim University, Saudi Arabia*
[d]*Faculty of Sciences, University of Sfax, LSME, Sfax 3018, Tunisia*
[e]*Department of Physics, Faculty of Science, Zagazig University Egypt, Egypt*
[f]*University of Coimbra, CFisUC, Physics Department, Rua Larga, 3004-516 Coimbra, Portugal*

in a net magnetization induced by an applied electric field and, conversely, an electric polarization induced by an external magnetic field.[25] The potential for ferroelectric ordering in polycrystalline rare-earth orthochromites with perovskite or distorted perovskite structures was first explored by Subba *et al.*[26] From resistivity-temperature and polarization measurements, indications of ferroelectric ordering have arisen in $DyCrO_3$, $YbCrO_3$, $HoCrO_3$, and $LuCrO_3$.[27] This behavior is attributed to distortions in the oxygen polyhedra surrounding Cr^{3+} ions. Additionally, these materials exhibit p-type extrinsic semiconducting behavior due to the presence of impurities such as Cr^{4+} or Cr^{6+} in their lattice.[28] Notably, bulk GCO exhibits multiple ferroelectric ordering transitions, with the first observed at 360 K and another at 425 K, above which the spontaneous polarization diminishes.[29] However, detailed dielectric properties below room temperature in the bulk regime remain unreported. Orthochromites are recognized for their high conductivity, robust chemical stability, and dense structure.[30] Recent studies have extensively explored the electrical, dielectric, and optical properties of several orthochromite compounds, such as $PrCrO_3$,[31,32] $SmCrO_3$,[33] $GdCrO_3$,[34] and $RFe_xCr_{1-x}O_3$.[35] These investigations have highlighted the emergence of notably high, sometimes colossal, permittivity, often attributed to effects related to grain boundaries.[36]

Below, we present a detailed investigation of the structural, electrical, and dielectric properties of GCO nanoparticle prepared by the sol–gel method.

2 Detailed experimentation

2.1 Sample preparation

Gadolinium and chromium nitrates (from Aldrich) were used to prepare $GdCrO_3$ (GCO) nanoparticles by the sol–gel method.[37–39] Sufficient amounts of each nitrate with the desired stoichiometric proportions were mixed and dissolved in distilled water. Citrate acid ($C_6H_8O_7$) was subsequently introduced as a chelating agent into the mixture with the molar ratio (metal ions): (citric acid) = 1 : 2. The solution was brought to 80 °C with magnetic stirring until the water evaporated. The gel formed at 180 °C is heated to 350 °C to obtain a dark powder. In order to eliminate all organic entities, the powder obtained was heated to 700 °C for 12 hours. Subsequently the product was finely ground, compressed into pellets of approximately 8 mm in diameter and 1 mm in thickness and heated at 800 °C for 4 hours to obtain the desired material.

2.2 Characterization

X-ray diffraction (XRD) was performed using a PANalytical diffractometer with Cu Kα1 radiation (λ = 1.5406 Å) over a 2θ range of 20° to 80°. The resulting XRD patterns were analyzed to determine the lattice parameters of the samples using the FullProf program and the Rietveld refinement method.[40] The morphology and chemical composition of the powder were examined using a TESCAN VEGA3 SBH scanning electron microscope (SEM) to evaluate the homogeneity of the $GdCrO_3$ compound. The TEM images were acquired using a high-resolution transmission electron microscope (HR-TEM) FEI Tecnai G2, operating at an accelerating voltage of 200 kV. Electrical measurements were conducted on a pellet with dimensions of 1 mm in thickness and 8 mm in diameter. Complex impedance measurements were carried out using a 'Solartron 1260' impedance analyzer over a frequency range of 10 Hz to 10^6 Hz at temperatures ranging from 153 K to 373 K with a configuration involving capacitance in parallel with resistance (C_p–R_p configuration).[41–43]

3 Results and discussions

3.1 XRD structural analysis

Fig. 1 shows the X-ray diffraction patterns of the GCO sample measured at room temperature. The patterns indicate a distorted perovskite structure with the *Pbnm* space group (JCPDS

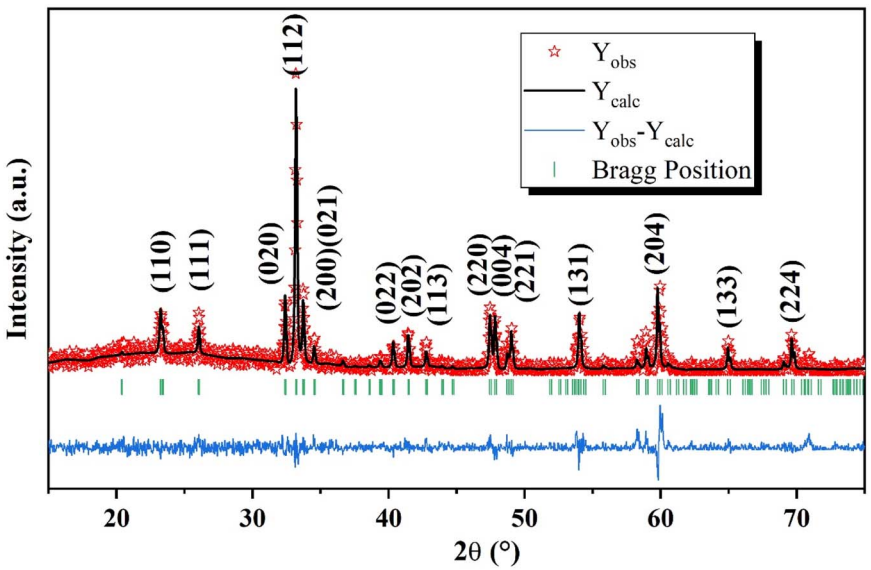

Fig. 1 X-ray diffraction patterns of GCO orthochromite perovskite oxide at room temperature.

Table 1 Lattice parameters of GCO orthochromite perovskite oxide derived from Rietveld refinement

	GCO
Space group	*Pbnm*
a (Å)	5.314_1
b (Å)	5.526_4
c (Å)	7.603_5
v (Å^3)	223.292_8
χ^2	1.034

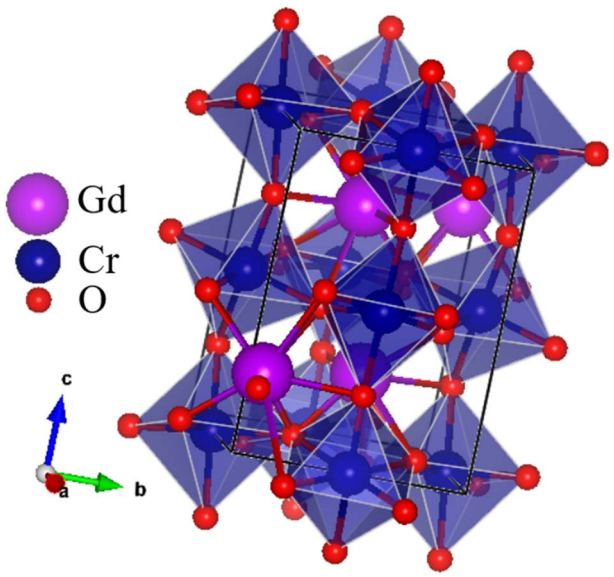

Fig. 2 Orthorhombic unit cell of GCO perovskite material modeled with Vesta Software.

COD. 34-0406).[44] The sharp peaks in the XRD patterns suggest that the samples are well-crystallized.[45] No impurity peaks were detected, confirming the high purity of the prepared samples.[46]

The lattice parameters of the GCO sample, determined through Rietveld refinement, are listed in Table 1. The reliability of the refinement model was assessed using discrepancy *R*-factors and goodness of fit, which demonstrated results within acceptable limits. The orthorhombic unit cell of the GCO perovskite material was created using Vesta software,[47–49] as shown in the inset of Fig. 2. This figure clearly illustrates the CrO_6 octahedra[50–52] and GdO_8 dodecahedra that make up the orthorhombic perovskite structure of the GCO compound.

3.2 Morphology analysis

The surface morphology of the $GdCrO_3$ (GCO) sample was analyzed using SEM, revealing a granular structure with interconnected particles, characteristic of polycrystalline perovskite materials (Fig. 3a). The particle size distribution was quantified using ImageJ software to process the SEM images, and the data were fitted to a Lorentzian distribution, as shown in the histogram (Fig. 3b), yielding an average particle size of 449 nm. This analysis indicates a relatively uniform particle size distribution, which is crucial for achieving consistent dielectric and electrical properties. Additionally, the observed morphology suggests the presence of a porous structure, which could influence the material's overall performance in electronic applications by affecting properties such as charge transport and dielectric behavior.

The internal structure and finer morphology of the $GdCrO_3$ (GCO) sample were investigated using TEM as shown in Fig. 4. The images reveal individual nanoparticles that appear larger than those observed in SEM, likely due to agglomeration effects. The nanoparticles exhibit irregular shapes, with some overlap, typical of materials synthesized by the Sol–gel method. While individual boundaries are discernible, the observed clustering suggests that inter-particle interactions during synthesis lead to aggregation. The TEM analysis indicates a relatively uniform internal composition and few crystalline defects, consistent

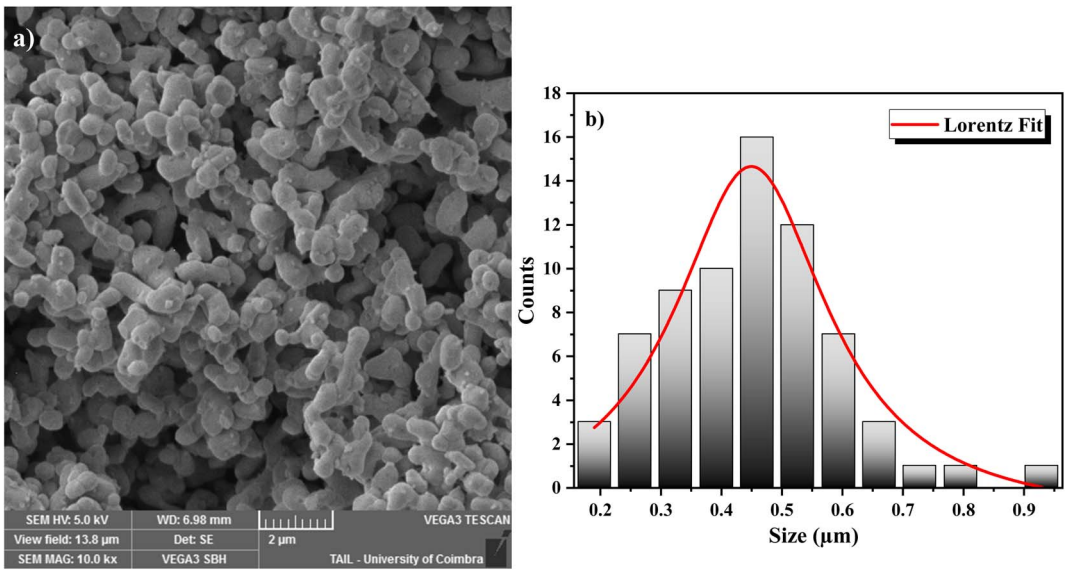

Fig. 3 (a) SEM image and (b) the average grains size histograms of $GdCrO_3$.

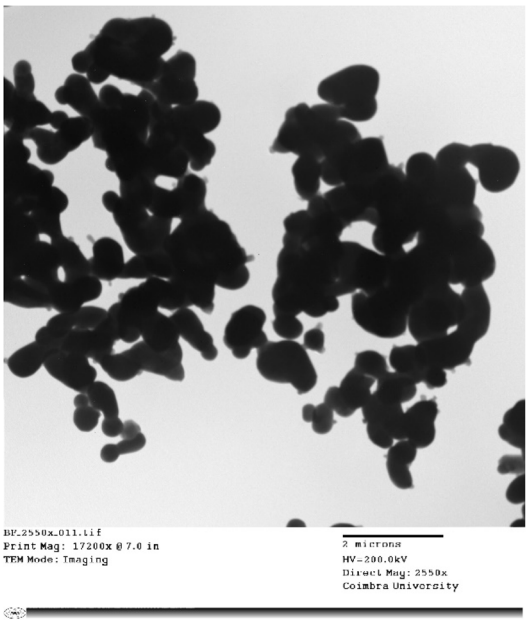

Fig. 4 TEM image of $GdCrO_3$.

with the expected perovskite structure. This agglomeration and nanoscale size may significantly influence the material's dielectric and electrical properties.

The EDX analysis of the $GdCrO_3$ (GCO) sample reveals the elemental composition of the material, confirming the presence of gadolinium (Gd), oxygen (O), and chromium (Cr) (Fig. 5). Table 2 summarizes the atomic and weight percentages of the elements present in the $GdCrO_3$ (GCO) sample, as determined by EDX analysis. The atomic percentages are 20.19% for Gd, 61.58% for O, and 18.23% for Cr, indicating a stoichiometric ratio that aligns well with the expected perovskite structure. In terms of weight percentages, gadolinium contributes 58.69%, while chromium and oxygen contribute 21.56% and 19.75%, respectively.

Table 2 Atomic (%) and Weight (%) of $GdCrO_3$

Elements	Series	Atomic (%)	Weight (%)
Gadolinium	L-series	20.19	58.69
Oxygen	K-series	61.58	19.75
Chromium	K-series	18.23	21.56
Total		100.00	100.00

3.3 Electrical conductivity analysis

Fig. 6 illustrates the frequency-dependent conductivity of GCO chromite at various temperatures from 153 K to 373 K. The analysis identifies two main regimes: at low frequencies, the conductivity remains constant, forming a plateau known as continuous conductivity. As the frequency increases, the conductivity shifts from this static regime to a dispersive regime, referred to as AC conductivity. This behavior follows Jonscher's classical law, which is expressed by the formula:[53]

$$\sigma_{ac} = \sigma_{dc} + A\omega^{s} \quad (1)$$

In this equation, σ_{dc} denotes the steady-state conductivity, A is a factor dependent on temperature, ω is the angular frequency, and **s** signifies the extent of interaction between the moving charges and their environment. According to Funke,[54] values of **s** less than 1 indicate a sudden jump in the translational motion of charges, while values greater than 1 suggest that charge carriers are jumping between neighboring localized sites. Additionally, this parameter helps determine the dominant conduction model. Depending on how **s** varies with temperature, different models can be identified: electronic or polaronic. If **s** decreases as temperature increases, the barrier-correlated hopping (CBH) model dominates.[55] When **s** increases with

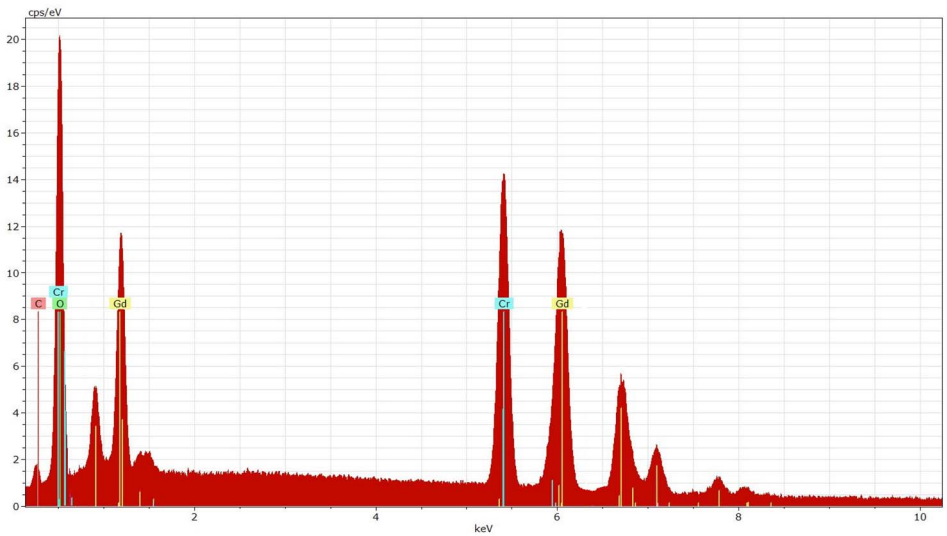

Fig. 5 EDX spectrum of $GdCrO_3$.

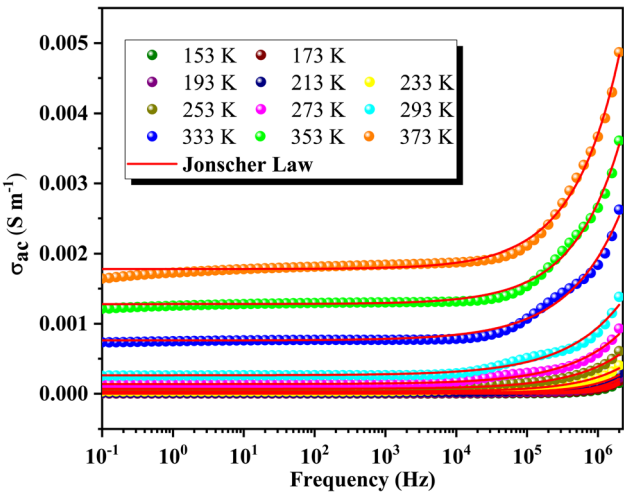

Fig. 6 Temperature-dependent conductivity spectra of GCO chromite.

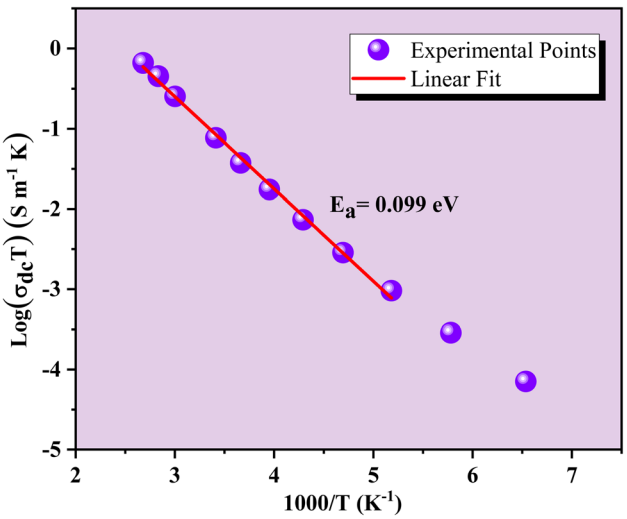

Fig. 8 Variation of $\log(\sigma_{dc}T)$ as a function of $1000/T$ for GCO compound.

temperature, the non-overlapping small polaron tunneling (NSPT) model governs conduction.[56] If **s** initially decreases to a minimum and then increases, the large overlapping polaron tunneling (OLPT) model is followed.[57] Lastly, the quantum mechanical tunneling (QMT) model applies when **s** remains constant near 0.81, regardless of temperature changes.[58] As shown in the insets of Fig. 7, the thermal variation of **s** indicates that the conduction mechanism is of polaronic origin and follows the OLPT model.

Fig. 8 shows the variations of $\log(\sigma_{dc}T)$ as a function of the inverse temperature for the GCO compound in the semiconductor region. The high-temperature dc conductivity data suggest that the conductivity is dominated by the small polaron hopping (SPH) mechanism. This is described by the Arrhenius equation:[59]

$$\sigma_{dc}T = \sigma_0 \exp(-E_a/K_BT) \quad (2)$$

In this equation, E_a is the activation energy, σ_0 is the pre-exponential factor, T is the absolute temperature, and K_B is the Boltzmann constant. The value of E_a is deduced from the slope of the linear fit plot using eqn (2). We obtained 0.099 eV for the GCO sample. This value of E_a indicates the energy required for charge carriers to hop between localized sites. It suggests that the conduction mechanism in the GCO sample involves significant interactions or potential barriers affecting the mobility of the charge carriers, which could be due to the intrinsic properties of the material such as lattice structure or defect states.

The evolution of $\log(\sigma_{ac}T)$ as a function of the inverse temperature is depicted in Fig. 9. These curves were utilized to validate the Arrhenius conduction mechanism in polarons' transport and determine activation energies (E_a) across various

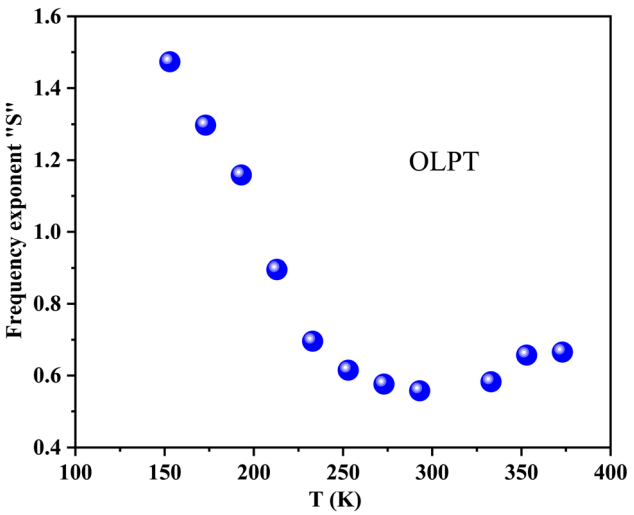

Fig. 7 Thermal variation of **s** indicating polaronic conduction *via* the OLPT model.

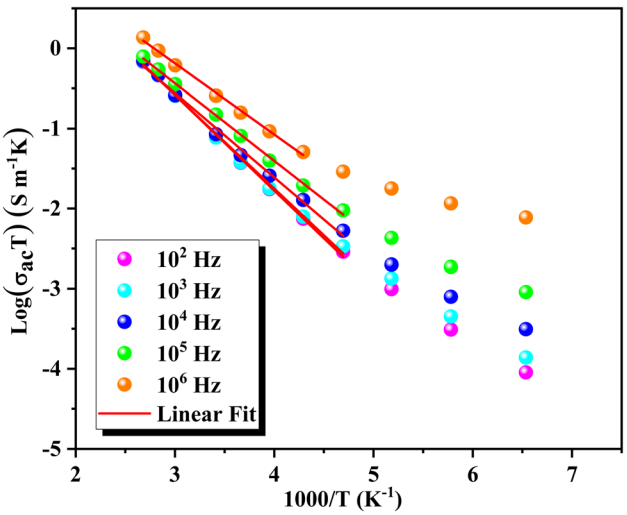

Fig. 9 Temperature dependence of $\log(\sigma_{ac}T)$ and Arrhenius activation energy for GCO compound across frequencies.

Table 3 Activation energy values for GCO compound

Frequency (Hz)	10^2	10^3	10^4	10^5	10^6
E_a (eV)	0.1	0.099	0.091	0.084	0.076

temperatures and frequencies. The slopes of these curves vary with both frequency and temperature, demonstrating the nuanced behavior of conductivity under different conditions. The fit of $\log(\sigma_{ac}T)$ *vs.* $1000/T$ reveals a decrease in the Arrhenius activation energy in the low-temperature regime. Table 3 summarizes the trend of decreasing activation energy (E_a) with increasing frequency. Additionally, the observed increase in dc conductivity with temperature indicates enhanced charge carrier mobility at higher temperatures. The combined effect of a decrease in E_a and a simultaneous increase in ac conductivity (σ_{ac}) with frequency suggests that hopping conduction is the dominant mechanism governing the electrical behavior of the material.[60]

3.4 Impedance analysis

Fig. 10 illustrates the variation of the real part of impedance (Z') with frequency at different temperatures. The plot reveals two distinct behaviors depending on frequency. Initially, Z' exhibits a plateau regardless of frequency, indicating a stable impedance at low frequencies. However, as frequency increases, Z' shows a significant decrease with rising temperature at specific frequencies. This observation correlates well with the continuous variation of conductivity observed at low frequencies, confirming the semiconductor characteristics of our compounds.[61] In the intermediate frequency range, higher frequencies lead to a reduction in the accumulation of charges at grain boundaries, thereby causing a decrease in Z'. At higher frequencies, the Z' spectra converge independently of frequency and temperature, indicating the dissipation of space charges due to reduced potential barriers.[62] This plateau in behavior can be explained by the fact that within this frequency range, the mobile charges reach their relaxation frequencies and can no longer respond to the external electrical excitation.

Fig. 11 shows the variation of the imaginary part of impedance Z'' with frequency at different temperatures. Each temperature curve exhibits two distinct relaxation peaks at specific frequencies. The peak at the lower frequency side corresponds to the hopping of charge carriers between sites at the grain boundaries. In contrast, the peak at the higher frequency side is associated with the short-range hopping of carriers between localized sites within the grains. Additionally, as the temperature increases, these two peaks shift towards higher frequencies, indicating that the relaxation process is thermally activated (*i.e.*, the dipoles are activated). Furthermore, the increase in temperature is accompanied by a decrease in the peak maxima, which can be attributed to the reduction in the electrical resistance of the compounds.

Fig. 12a and b presents Nyquist plots for the GCO compound across a range of temperatures (153–373 K). The Cole–Cole plots display two distinct semicircles, whose diameters decrease with increasing temperature. These diameters are indicative of the compound's resistance. As the temperature rises, the shrinking semicircle diameters suggest that the conduction process is thermally activated, thus confirming the semiconductor nature of the sample.[63] The presence of two semicircular arcs indicates the existence of two distinct relaxation phenomena. The Cole–Cole plots were analyzed using Z-view software,[64] employing various equivalent circuit models as shown in Fig. 12a and b. For the temperature range of 153 K to 213 K (Fig. 12a), the optimal fit was obtained with an equivalent circuit that includes a series combination of three elements: the electrode (R_e//CPEe), the grain boundaries (R_{gb}//CPEgb), and the grain (R_g//C_g). In the higher temperature range of 233 K to 377 K, depicted in Fig. 12b, the equivalent circuit configuration is represented as [R_s + (R_g//CPEg) + (R_{gb}//CPEgb) + (R_e//CPEe)], where R represents resistance and CPE stands for constant phase element. However, some curves do not reach zero in the low-frequency range for temperatures above 213 K. This phenomenon may

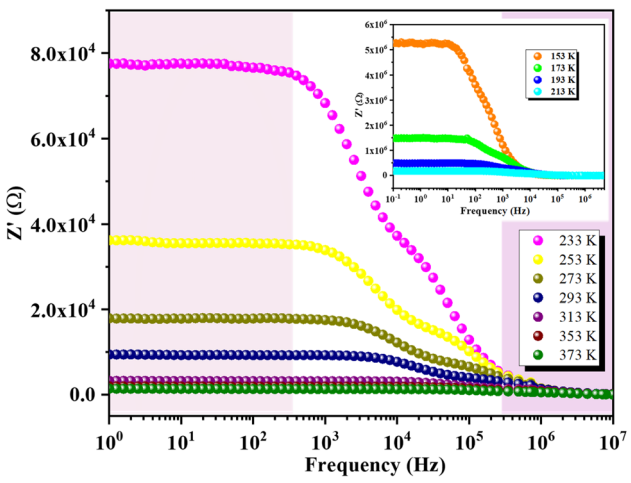

Fig. 10 Frequency-dependent impedance behavior in GCO compound.

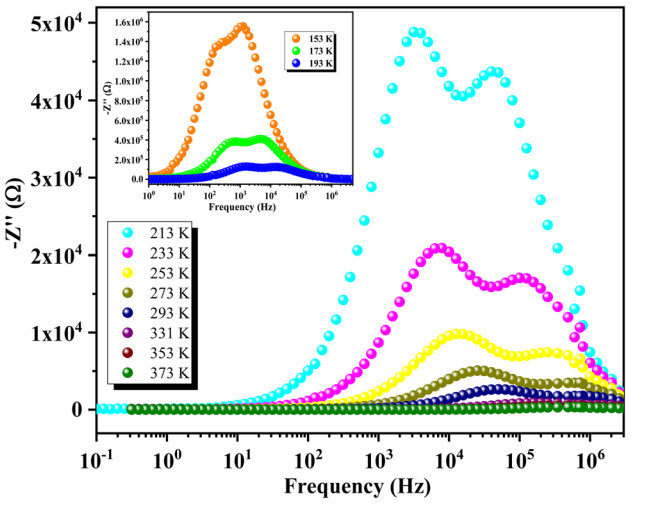

Fig. 11 Frequency-dependent imaginary impedance Z'' showing double relaxation peaks in GCO compound.

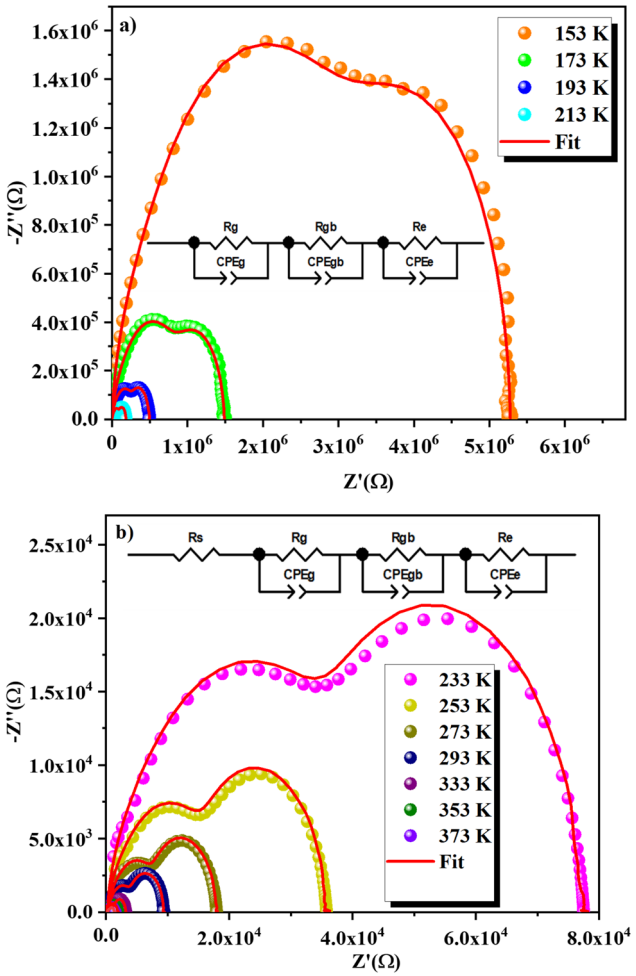

Fig. 12 Nyquist plots of GCO compound at various temperatures, (a) 153–213 K and (b) 233–373 K.

be due to interface effects at low frequencies or could be attributed to the addition of resistance R_s, which prevents the curves from reaching zero in this range.

The activation energy can be determined using the Arrhenius equation:

$$R_{s,g,gb,e}(\Omega) = R_0 e^{-E_a/K_B T} \quad (3)$$

where K_B is the Boltzmann constant, R_0 represents the pre-exponential constant or characteristic resistance and E_a is the activation energy. The logarithmic variation of R_s, R_g, R_{gb} and R_e as a function of the inverse of the temperature is shown in Fig. 13. Table 4 presents activation energy values for electrode, grain, grain boundaries, and grain resistance. The activation energy for the grain (0.083 eV) is higher than that for the grain boundaries (0.079 eV), indicating that the conduction process encounters more resistance within the grains than at the grain boundaries.

3.5 Modulus analysis

The variation of the real part of the modulus M' as a function of frequency at different temperatures is depicted in Fig. 14. At

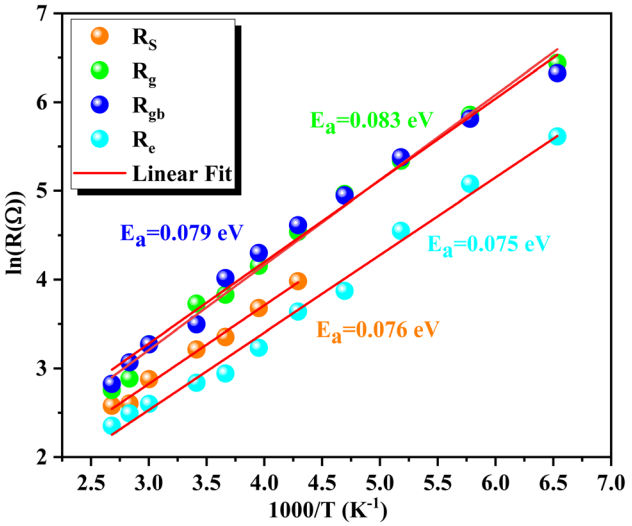

Fig. 13 Logarithmic variation of R_s, R_g, R_{gb} and R_e with inverse temperature.

Table 4 Activation energy values for electrode, grain, grain boundaries, and grain resistance

Parameter	R_s (Ω)	R_g (Ω)	R_{gb} (Ω)	R_e (Ω)
E_a (eV)	0.076	0.083	0.079	0.075

lower temperatures, M' shows a continuous increase with frequency. In contrast, at higher temperatures, M' initially exhibits a static behavior at low frequencies, followed by an increase to an intermediate frequency where it stabilizes at a frequency-independent value. Each M' spectrum of GCO perovskite demonstrates an increasing trend with frequency, reaching a saturation value M_∞ that reflects short-range mobility of charge carriers in the material's electrical transport mechanism. Additionally, M' values decrease uniformly

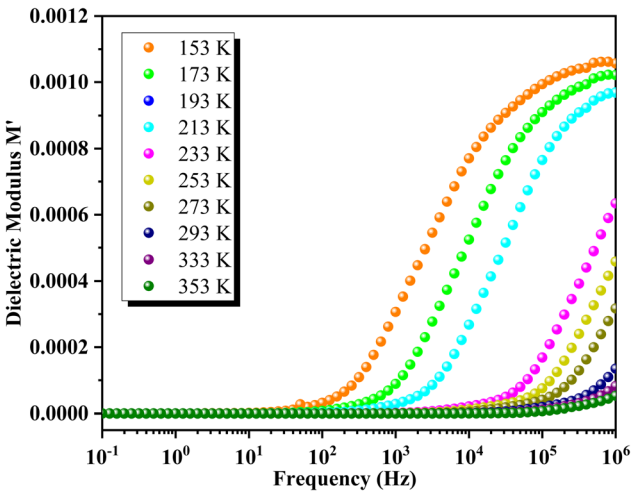

Fig. 14 Frequency dependence of the real part of modulus M' at different temperatures.

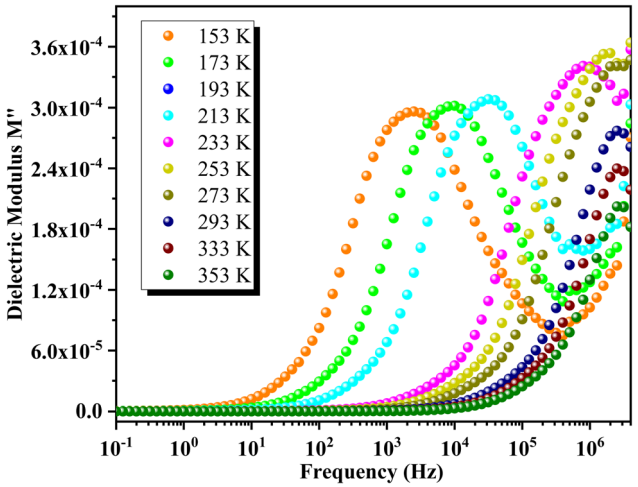

Fig. 15 Frequency dependence of M'' at various temperatures for GCO.

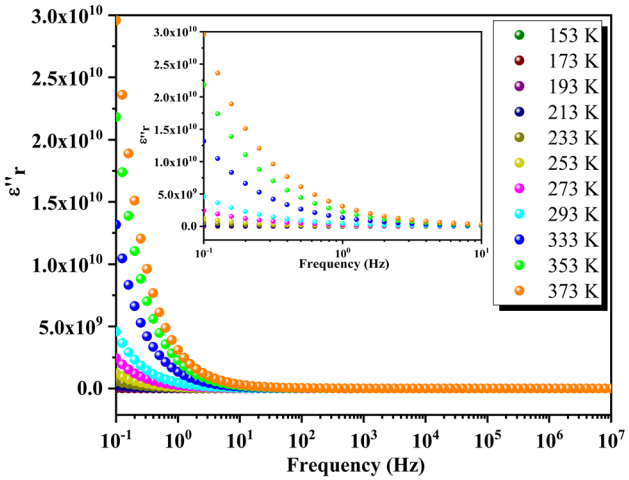

Fig. 17 Frequency dependence of imaginary permittivity in GCO compound.

with rising temperature across all frequencies, indicating the presence of temperature-dependent relaxation phenomena in GCO material's electrical conduction.

Fig. 15 illustrates the frequency dependence of M'' at various temperatures for GCO. Each curve exhibits a distinct asymmetric relaxation peak located at intermediate frequencies, indicative of grain-related effects. As temperature increases, the peak maximum shifts towards higher frequencies, suggesting a decrease in relaxation time.

3.6 Permittivity analysis

Fig. 16 depicts the frequency-dependent behavior of the real part of permittivity at various temperatures. At lower frequencies, the permittivity shows higher values, influenced by grain size effects and various polarization mechanisms such as dipolar, ionic, electronic and interfacial polarizations.[65] As the frequency increases, the permittivity gradually decreases and eventually stabilizes at a lower constant value at higher frequencies, indicating the presence of space charges. At lower temperatures, ε' decreases uniformly with frequency, while at higher temperatures, ε' stabilizes at low frequencies before rapidly decreasing beyond a certain threshold. This behavior indicates an increase in the density of mobile charges and/or the difficulty electric dipoles encounter in responding to the applied electric excitation.

In Fig. 17, the frequency dependence of the imaginary part of the permittivity at different temperatures is illustrated. As the frequency increases, ε'' exhibits a rapid decrease until it reaches a minimum value at frequencies around 10 Hz. Beyond this point, ε'' shows insensitivity to further increases in frequency and temperature. This behavior is attributed to Koop's theory and the Maxwell–Wagner phenomenological model, which explain that the dielectric structure of these compounds is characterized by grains with high conductivity that are

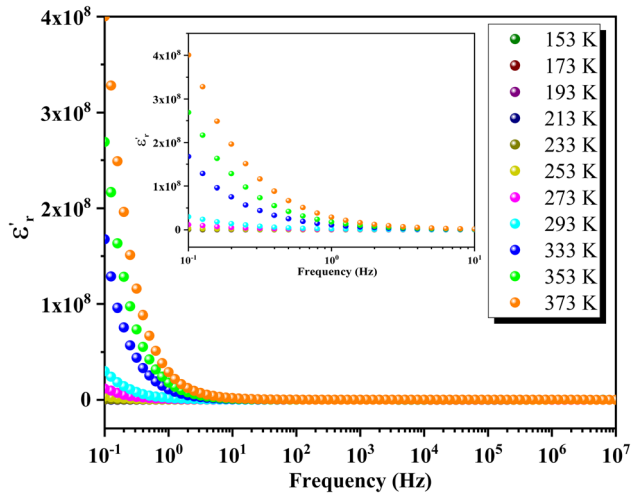

Fig. 16 Frequency-dependent behavior of permittivity in GCO perovskite at various temperatures.

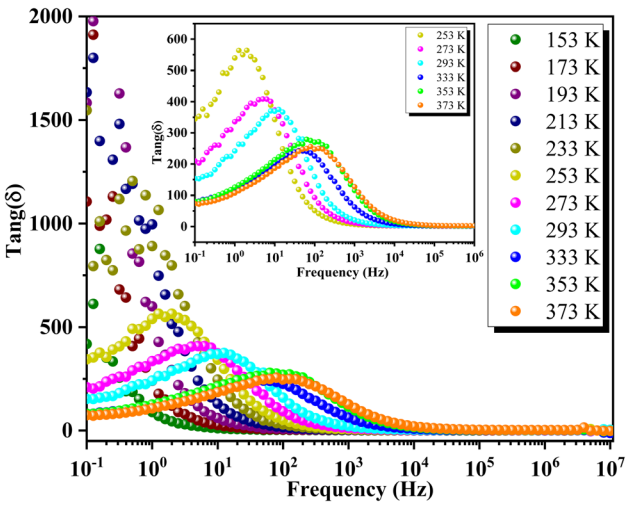

Fig. 18 Frequency-dependent dielectric loss (tan $g(\delta)$) of GCO chromite across different temperatures.

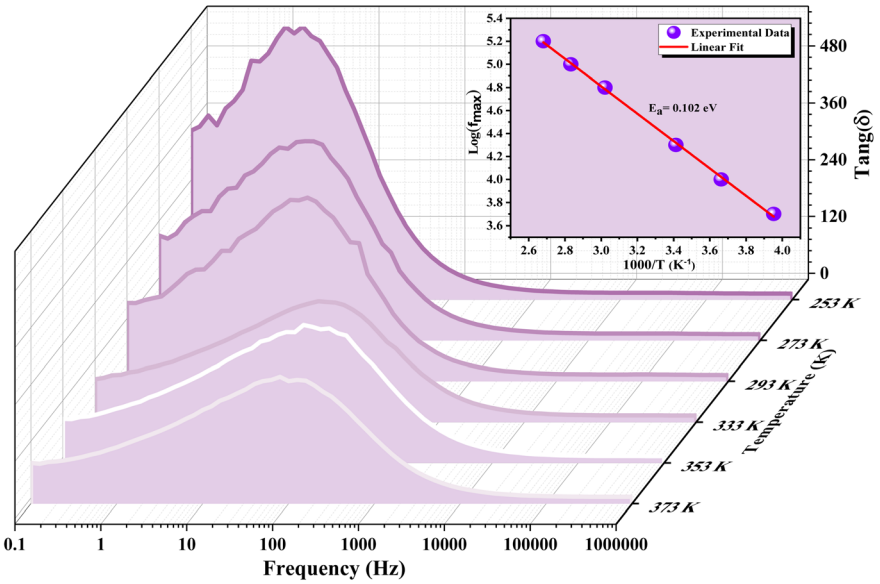

Fig. 19 Dielectric loss characteristics and activation energy analysis of GCO chromite.

particularly effective at higher frequencies. Fig. 18 illustrates the frequency-dependent variation of dielectric loss (tan(δ)) in GCO chromite across different temperatures. At lower frequencies, tan(δ) exhibits higher values, which can be attributed to interfacial effects, before decreasing to a minimum within each temperature spectrum. The dielectric loss spectra demonstrate significant temperature-dependent variations, with substantial losses observed at different temperature ranges. These losses are likely due to defect states, such as oxygen vacancies and mixed valence states, contributing to the highly disordered nature of the material. The multiple peaks and shifts in the spectra across various temperatures highlight the complexity of the material's dielectric response. These insights into the structural and functional properties of GCO chromite underscore its potential for applications in electronic and electrical devices, where controlled conductivity and dielectric properties are essential.

However, tan $g(\delta)$ exhibits an upward trend in the intermediate frequency range, peaking at the relaxation frequency (f_{max}), before declining with further frequency increments. The presence of these peaks at fmax across temperatures from 253 K to 373 K suggests the occurrence of thermally activated hopping phenomena within the GCO perovskite structure. However, the loss peak shifts to higher frequencies as temperatures rise, indicating a decrease in relaxation time. The temperature dependency of f_{max} follows an Arrhenius-like relationship expressed as:

$$f_{max} = f_0 e^{-E_a/K_B T} \quad (4)$$

where E_a denotes the activation energy for relaxation, f_0 represents the pre-exponential factor. Fig. 19 illustrates the 3D frequency-dependent dielectric loss (tan $g(\delta)$) of GCO chromite at various temperatures. Inset: plot of ln(f_{max}) *versus* the inverse of temperature, with the red line representing the fitted peak frequency Arrhenius equation. The activation energy estimated from the dielectric loss spectra is 102 meV. The significant dielectric loss observed in GCO perovskite indicates its highly disordered nature, likely influenced by defect states such as oxygen vacancies and mixed valence.

4 Conclusion

In conclusion, the study of GCO compounds, particularly their electrical and dielectric properties, has revealed several key insights. The perovskite phase of GCO, confirmed through X-ray diffraction analysis, crystallizes with the *Pbnm* space group, underscoring its structural integrity and potential for diverse applications. Scanning electron microscopy (SEM) and energy-dispersive X-ray spectroscopy (EDX) analyses demonstrated the morphology and chemical composition of GCO, confirming its homogeneity and validating the synthesis process. Additionally, transmission electron microscopy (TEM) provided insights into the finer internal structure of the material. Electrical characterization has shown that GCO exhibits semiconductor behavior, with temperature-dependent conductivity suggesting thermally activated processes dominated by hopping conduction mechanisms. GCO is a material with giant permittivity (10^8) and low energy losses for temperatures above 253 K, making it an excellent candidate for energy storage. The activation energies extracted from various analyses provide crucial insights into charge carrier mobility and relaxation dynamics within GCO. Overall, these findings underscore GCO's potential for applications in electronic and electrical devices where controlled conductivity and dielectric properties are essential.

Data availability

Data are available upon request to the authors.

Conflicts of interest

The authors declare that they have no known competing financial interests or personal relationships that could have appeared to influence the work reported in this paper.

References

1 H. Zhang, Y. Bian, Y. Xia, Y. Cui, Z. Li, F. Zhang, Y. Bai, N. Chen and J. Chen, Correlated perovskite nickelates with valence variable rare-earth compositions, *J. Rare Earths*, 2024, **42**(4), 743–748.

2 R. Roy and A. Dutta, Structural, optical, electrical, and dielectric relaxation properties of rare earth containing sodium bismuth titanate $Na_{0.5}Bi_{0.5}TiO_3$ perovskite: Effect of ionic radius, *J. Rare Earths*, 2024, **42**(2), 383–391.

3 S. Supriya, Recent trends and morphology mechanisms of rare-earth based $BiFeO_3$ nano perovskites with excellent photocatalytic performances, *J. Rare Earths*, 2023, **41**(3), 331–341.

4 M. Javed, A. A. Khan, J. Kazmi, N. Akbar, S. N. Khisro, A. Dar, A. D. K. Tareen and M. A. Mohamed, Variable range hopping transport and dielectric relaxation mechanism in $GdCrO_3$ rare-earth orthochromite perovskite, *J. Rare Earths*, 2024, **42**(7), 1304–1316.

5 J. R. Sahu, C. R. Serrao, N. Ray, U. V. Waghmare and C. N. R. Rao, Rare earth chromites: a new family of multiferroics, *J. Mater. Chem.*, 2007, **17**, 42–44.

6 I. Bhati, P. B. Punjabi and S. C. Ameta, Photocatalytic degradation of fast green using nanosized $CeCrO_3$, Maced, *J. Chem. Chem. Eng.*, 2010, **29**, 195.

7 K. Yoshii and A. Nakamura, Reversal of magnetization in $La_{0.5}Pr_{0.5}CrO_3$, *J. Solid State Chem.*, 2000, **155**(2), 447–450.

8 A. Indra, K. Dey, A. Midya, P. Mandal, O. Gutowski, U. Rütt, S. Majumdar and S. Giri, Magnetoelectric coupling and exchange bias effects in multiferroic $NdCrO_3$, *J. Phys.: Condens.Matter*, 2016, **28**(16), 166005.

9 T. Yamaguchi and K. Tsushima, Magnetic symmetry of rare-earth orthochromites and orthoferrites, *Phys. Rev. B*, 1973, **8**, 5187.

10 T. Arakawa, S. Tsuchi-Ya and J. Shiokawa, Catalytic activity of rare-earth orthoferrites and orthochromites, *Mater. Res. Bull.*, 1981, **16**(1), 97–103.

11 J. Mao, Y. Sui, X. Zhang, Y. Su, X. Wang, Z. Liu, Y. Wang, R. Zhu, Y. Wang, W. Liu and J. Tang, Temperature-and magneticfield-induced magnetization reversal in perovskite $YFe_{0.5}Cr_{0.5}O_3$, *Appl. Phys. Lett.*, 2011, **98**(19), 192510.

12 V. V. Kharton, A. A. Yaremchenko and E. N. Naumovich, Research on the electrochemistry of oxygen ion conductors in the former Soviet Union. II. Perovskite-related oxides, *J. Solid State Electrochem.*, 1999, **3**, 303–326.

13 Z. Shao, W. Zhou and Z. Zhu, Advanced synthesis of materials for intermediate temperature solid oxide fuel cells, *Prog. Mater. Sci.*, 2012, **57**(4), 804–874.

14 M. Siemons, A. Leifert and U. Simon, Preparation and gas sensing characteristics of nanoparticulate p-type semiconducting $LnFeO_3$ and $LnCrO_3$ materials, *Adv. Funct. Mater.*, 2007, **17**(13), 2189–2197.

15 A. McDannald, L. Kuna and M. Jain, Magnetic and magnetocaloric properties of bulk dysprosium chromite, *J. Appl. Phys.*, 2013, **114**(11), 113904.

16 R. Saha, A. Sundaresan and C. N. R. Rao, Novel features of multiferroic and magnetoelectric ferrites and chromites exhibiting magnetically driven ferroelectricity, *Mater. Horiz.*, 2014, **1**, 20–31.

17 Z. Hou, F. Chen, J. Wang, C. P. François-Xavier and T. Wintgens, Novel $Pd/GdCrO_3$ composite for photo-catalytic reduction of nitrate to N_2 with high selectivity and activity, *Appl. Catal., B*, 2018, **232**, 124–134.

18 K. Parida, A. Nashim and S. K. Mahanta, Visible-light driven $Gd_2Ti_2O_7/GdCrO_3$ composite for hydrogen evolution, *Dalton Trans.*, 2011, **40**(48), 12839–12845.

19 S. Mahana, U. Manju and D. Topwal, $GdCrO_3$: a potential candidate for low temperature magnetic refrigeration, *J. Phys. D: Appl. Phys.*, 2018, **51**(30), 305002.

20 A. Nashim, S. Pany and K. Parida, Systematic investigation on the charge storage behavior of $GdCrO_3$ in aqueous electrolyte, *J. Energy Storage*, 2021, **42**, 103145.

21 S. Terkhi, S. Bentata, Z. Aziz, T. Lantri and B. Abbar, First principle calculations of structural, electronic and magnetic properties of cubic $GdCrO_3$ Perovskite, *Indian J. Phys.*, 2018, **92**, 847–854.

22 S. Mahana, U. Manju and D. Topwal, Complex magnetic behavior in $GdCrO_3$, *AIP Conf. Proc.*, 2017, **1832**(1), 130046.

23 A. Jaiswal, R. Das, S. Adyanthaya and P. Poddar, Synthesis and optical studies of $GdCrO_3$ nanoparticles, *J. Nanopart. Res.*, 2011, **13**, 1019–1027.

24 T. Yamaguchi and K. Tsushima, Magnetic symmetry of rare-earth orthochromites and orthoferrites, *Phys. Rev. B*, 1973, **8**, 5187–5198.

25 T. Yamaguchi and K. Tsushima, Magnetic Symmetry of Rare-Earth Orthochromites and Orthoferrites, *Phys. Rev. B*, 1973, **8**, 5187.

26 G. V. Subba Rao, G. V. Chandrashekhar and C. N. R. Rao, Are rare earth orthochromites ferroelectric?, *Solid State Commun.*, 1968, **6**(3), 177–179.

27 A. Jaiswal, R. Das, K. Vivekanand, T. Maity, P. M. Abraham, S. Adyanthaya and P. Poddar, Magnetic and dielectric properties and Raman spectroscopy of $GdCrO_3$ nanoparticles, *J. Appl. Phys.*, 2010, **107**, 013912.

28 A. K. Tripathi and H. B. Lal, Electrical transport in light rare-earth orthochromites, *J. Mater. Sci.*, 1982, **17**, 1595–1609.

29 H. B. Lal, R. D. Dwivedi and K. Gaur, Pyroelectric and dielectric properties of some light rare-earth orthochromites, *J. Mater. Sci.: Mater. Electron.*, 1990, **1**, 204–208.

30 Y. Shen, M. Liu, T. He and S. P. Jiang, electrical conductivity, and thermal expansion behavior of dense $Nd_{1-x}Ca_xCrO_3$ solid solutions, *J. Am. Ceram. Soc.*, 2009, **92**, 2259–2264.

31 R. Mguedla, A. Ben Jazia Kharrat, M. Saadi, K. Khirouni, N. Chniba-Boudjada and W. Boujelben, Structural, electrical, dielectric and optical properties of $PrCrO_3$ orthochromite, *J. Alloys Compd.*, 2020, **812**, 152130.

32 R. Mguedla, A. Ben Jazia Kharrat, O. Taktak, H. Souissi, S. Kammoun, K. Khirouni and W. Boujelben, Experimental and theoretical investigations on optical properties of multiferroic $PrCrO_3$ ortho chromite compound, *Opt. Mater.*, 2020, **101**, 109742.

33 Z. Xiang, J. Xub, Y. Huang, S. Gea and Y. Cui, Novel multiferroicity in orthorhombic $SmCrO_3$, *Nat. Sci. Mater.*, 2018, **28**, 609–613.

34 J. Shanker, K. Venkataramana, B. Vittal Prasad, R. Vijaya Kumar and D. Suresh Babu, Influence of Fe substitution on structural and electrical properties of Gd orthochromite ceramics, *J. Alloys Compd.*, 2018, **732**, 314–327.

35 J. Shanker, B. Vittal Prasad, M. Buchi Suresh, R. Vijaya Kumar and D. Suresh Babu, Electrical properties of $NdCr_{1-x}Fe_xO_3$ perovskite ceramic nanoparticles-An impedance spectroscopy studies Mater, *Res. Bull.*, 2017, **94**, 385–398.

36 F. Rehman, J. B. Li, Y. K. Dou, J. S. Zhang, Y. J. Zhao, M. Rizwan, S. Khalid and H.-B. Jin, Dielectric relaxations and electrical properties of Aurivillius $Bi_{3.5}La_{0.5}Ti_2Fe_{0.5}Nb_{0.5}O_{12}$ ceramics, *J. Alloys Compd.*, 2016, **654**, 315–320.

37 A. Bougoffa, A. Benali, M. Bejar, E. Dhahri, M. P. F. Graça, M. A. Valente, L. Bessais and B. F. O. Costa, Mg-substitution effect on microstructure, dielectric relaxation and conduction phenomenon of Fe based perovskite nanomaterials, *J. Alloys Compd.*, 2021, **856**, 157425.

38 A. Benali, E. M. Benali, S. Gouadria, M. Elhadi, E. Dhahri, M. P. F. Graça, M. A. Valente and B. F. O. Costa, Colossal dielectric constant with enhanced magnetization in the La^{3+} and Ca^{2+} co-doped $BiFeO_3$ nanoparticles, *J. Mater. Sci.: Mater. Electron.*, 2022, **33**, 16236–16250.

39 I. Elhamdi, F. Mselmi, H. Souissi, S. Kammoun, E. Dhahri, P. Sanguino and B. F. O. Costa, Summerfield scaling model and electrical conductivity study for understanding transport mechanisms of a Cr^{3+} substituted $ZnAl_2O_4$ ceramic, *RSC Adv.*, 2023, **13**, 3377–3393.

40 H. M. Rietveld, A profile refinement method for nuclear and magnetic structures, *J. Appl. Crystallogr.*, 1969, **2**, 65–71.

41 A. Bougoffa, E. M. Benali, A. Benali, M. Bejar, E. Dhahri, M. P. F. Graça, M. A. Valente, G. Otero-Iruruetac and B. F. O. Costa, Investigation of temperature and frequency dependence of the dielectric properties of multiferroic $(L_{0.8}Ca_{0.2})_{0.4}Bi_{0.6}FeO_3$ nanoparticles for energy storage application, *RSC Adv.*, 2022, **12**, 6907–6917.

42 E. M. Benali, A. Benali, M. Bejar, E. Dhahri, M. P. F. Graca, M. A. Valente and B. F. O. Costa, Structural, morphological, Raman, dielectric and electrical properties of $La_{1-2x}Ba_xBi_xFeO_3$ ($0.00 \leq x \leq 0.20$) compounds, *RSC Adv.*, 2021, **11**, 36148–36165.

43 M. Horchani, A. Omri, M. Seif Eddine, A. Benali, A. Tozri, E. Dhahri, K. Pavani, B. F. O. Costa and M. F. P. Graca, Ni–Cu–Co ferrite synthesized using the sol–gel method: Effects of the Cr^{3+} ion concentration on its structural, electrical, and dielectric properties, *Appl. Phys. A*, 2022, **128**, 947.

44 A. Jaiswal, R. Das, S. Adyanthaya and P. Poddar, Synthesis and optical studies of $GdCrO_3$ nanoparticles, *J. Nanopart. Res.*, 2011, **13**, 1019–1027.

45 P. Mohanty, B. S. Jacobs, A. R. E. Prinsloo and C. J. Sheppard, Thermal decomposition of $GdCrO_4$ to $GdCrO_3$: structure and magnetism, *AIP Adv.*, 2021, **11**(1), 015235.

46 Z. Ma, G. Liu, W. Gao, Y. Liu, L. Xie, X. He, L. Liu, Y. Li and H. Zhang, The tunable spin reorientation, temperature induced magnetization reversal, and spontaneous exchange bias effect of $Sm_{0.7}Y_{0.3}Cr_{1-x}Ga_xO_3$, *RSC Adv.*, 2018, **8**, 33487–33495.

47 A. Heydon, J. Horning, R. Levin, T. Mann, and Y. Yu, *The Vesta-2 Software Description Language*, Technical Report 1997-005, 1997.

48 I. Elhamdi, H. Souissi, O. Taktak, S. Kammoun, E. Dhahri, J. Pina, B. F. O. Costa and E. López-Lago, Optical characterization and defect-induced behavior in $ZnAl_{1.999}Ho_{0.001}O_4$ spinel: Unraveling novel insights into structure, morphology, and spectroscopic features, *Heliyon*, 2024, **10**(8), e29241.

49 I. Elhamdi, H. Souissi, O. Taktak, J. Elghoul, S. Kammoun, E. Dhahri and B. F. O. Costa, Experimental and modeling study of ZnO: Ni nanoparticles for near-infrared light emitting diodes, *RSC Adv.*, 2022, **12**, 13074–13086.

50 I. Elhamdi, F. Mselmi, S. Kammoun, E. Dhahri, A. J. Carvalho, P. Tavares and B. F. O. Costa, A far-red-emitting $ZnAl_{1.95}Cr_{0.05}O_4$ phosphor for plant growth LED applications, *Dalton Trans.*, 2023, **52**, 9301–9314.

51 I. Elhamdi, H. Souissi, S. Kammoun, E. Dhahri, A. L. B. Brito, R. Fausto and B. F. O. Costa, Experimental determination and modeling of structural, vibrational and optical properties of the $ZnAl_{2-x}Cr_xO_4$ (x= 0 and 0.05) spinels, *J. Lumin.*, 2023, **263**, 119968.

52 I. Elhamdi, H. Souissi, S. Kammoun, E. Dhahri, J. Pina, B. F. O. Costa and E. López-Lago, Comprehensive characterization and optoelectronic significance of Ho^{3+} and Cr^{3+} Co-doped $ZnAl_2O_4$ spinels, *Dalton Trans.*, 2024, **53**, 7721–7733.

53 K. Weron, How to obtain the universal response law in the Jonscher screened hopping model for dielectric relaxation, *J. Phys.: Condens. Matter*, 1991, **3**, 221.

54 K. Funke, Jump relaxation in solid electrolytes, *Prog. Solid State Chem.*, 1993, **22**, 111–195.

55 R. B. Said, B. Louati, K. Guidara and S. Kamoun, Thermodynamic properties and application of CBH model in the ac conductivity of $LiNi_{1.5}P_2O_7$ ceramic, *Ionics*, 2014, **20**, 1071–1078.

56 A. Ghosh, Transport properties of vanadium germanate glassy semiconductors, *Phys. Rev. B*, 1990, **42**, 5665.

57 M. F. Kotkata, F. A. Abdel-Wahab and H. M. Maksoud, Investigations of the conduction mechanism and relaxation properties of semiconductor Sm doped a-Se films, *J. Phys. D: Appl. Phys.*, 2006, **39**, 2059.

58 S. R. Majid and A. K. Arof, Electrical behavior of proton-conducting chitosan-phosphoric acid-based electrolytes, *Phys. B*, 2007, **390**, 209–215.

59 K. P. Padmasree, D. K. Kanchan and A. R. Kulkarni, Impedance and Modulus studies of the solid electrolyte system 20CdI2–80 [xAg_2O–y ($0.7V_2O5$–0.3 B_2O_3)], where 1≤ x/y≤ 3, *Solid State Ionics*, 2006, **177**, 475–482.

60 M. Pecovska-Gjorgjevich, S. Aleksovska, S. Dimitrovska-Lazova and M. Marinšek, The role of Cr/Co substitution on dielectric properties of gadolinium orthochromite, *Phys. Scr.*, 2016, **91**, 045805.

61 P. B. Macedo, C. T. Moynihan and R. Bose, The role of ionic diffusion in polarisation in vitreous ionic conductors, *Phys. Chem. Glasses*, 1972, **13**, 171–179.

62 J. H. Joshi, G. M. Joshi, M. J. Joshi, H. O. Jethva and K. D. Parikh, Complex impedance, FT-Raman, and photoluminescence spectroscopic studies of pure and L-phenylalanine doped ammonium dihydrogen phosphate single crystals: the correlation with hydrogen bonding defect, *New J. Chem.*, 2018, **42**, 17227–17249.

63 M. Satalkar, S. N. Kane, M. Kumaresavanji and J. P. Araujo, On the role of cationic distribution in determining magnetic properties of $Zn_{0.7-x}Ni_xMg_{0.2}Cu_{0.1}Fe_2O_4$ nano ferrite, *Mater. Res. Bull.*, 2017, **91**, 14–21.

64 J. G. Lyagaeva, G. K. Vdovin and D. A. Medvedev, Distinguishing Bulk and Grain Boundary Transport of a Proton-Conducting Electrolyte by Combining Equivalent Circuit Scheme and Distribution of Relaxation Times Analyses, *J. Phys. Chem. C*, 2019, **123**(36), 21993–21997.

65 S. G. Kakade, Y.-R. Ma, R. S. Devan, Y. D. Kolekar and C. V. Ramana, Dielectric, Complex Impedance, and Electrical Transport Properties of Erbium (Er^{3+}) Ion-Substituted Nanocrystalline, Cobalt-Rich Ferrite ($Co_{1.1}Fe_{1.9-x}Er_xO_4$), *J. Phys. Chem. C*, 2016, **120**, 5682–5693.